

A Random Walk Model for Dark Matter Halo Concentrations

Turner Johnson¹, Andrew J. Benson^{2*}, Daniel Grin¹

¹ *Department of Physics and Astronomy, Haverford College, 370 Lancaster Avenue, Haverford, Pennsylvania 19041, USA*

² *Carnegie Observatories, 813 Santa Barbara Street, Pasadena, CA 91101, USA*

30 June 2020

ABSTRACT

We describe an algorithm for predicting the concentrations of dark matter halos via a random walk in energy space. Given a full merger tree for a halo, the total internal energy of each halo in that tree is determined by summing the internal and orbital energies of progenitor halos. For halos described by single-parameter density profiles (such as the NFW profile) the energy can be directly mapped to a scale radius, and so to a concentration. We show that this model can accurately reproduce the mean of the concentration mass relation measured in N-body simulations, and reproduces more of the scatter in that relation than previous models. However, our model underpredicts the kurtosis of the distribution of N-body concentrations. We test this model by examining both the autocorrelation of scale radii across time, and the correlations between halo concentration and spin, and comparing to results measured from cosmological N-body simulations. In both cases we find that our model closely matches the N-body results. Our model is implemented within the open source GALACTICUS toolkit.

Key words: dark matter – large-scale structure of Universe – cosmology: theory

1 INTRODUCTION

It has long been established that dark matter halos forming in a universe dominated by cold dark matter have a “universal” density profile [Bellovary et al. \(2008\)](#). This is often described by the NFW functional form [Navarro et al. \(1997\)](#), or, more recently, by the Einasto profile [Einasto \(1965\)](#); see, for example, [Navarro et al. 2004](#)). The universality has been explained using a radial orbit instability, as in [Navarro et al. \(1997\)](#), or adiabatic contraction near the peaks of Gaussian density fields, as in [Dalal et al. \(2010\)](#).

Given a halo mass, defined as the mass within some sphere or isodensity surface enclosing a given density contrast, the NFW profile is characterized by a single parameter, the scale radius, r_s , often parameterized in terms of the concentration, $c = r_v/r_s$, where r_v is the virial radius of the halo.

Understanding how the concentration is related to halo properties (such as the halo mass, formation time, etc.) is important for a number of theoretical and observational reasons. For example:

- more concentrated halos are expected to be able to survive longer in tidal fields ([Jiang et al. 2020](#)), thereby affect-

ing the number of surviving subhalos found around galaxies and within clusters;

- concentration has been shown to be a good predictor of galaxy sizes in hydrodynamical simulations of galaxy formation ([Jiang et al. 2019](#));

- concentration directly affects a halo’s cross section for gravitational lensing, making it an important ingredient in analyses of strong lensing systems which aim to constrain the particle nature of dark matter ([Gilman et al. 2019, 2020](#)).

It has been long established ([Navarro et al. 1996](#)) that this scale radius is closely correlated with the formation history of a halo, with earlier-forming halos being more concentrated (larger c , smaller r_s) than halos forming later at fixed halo mass. This correlation of concentration with the assembly history of a halo was further explored by [Bullock et al. \(2001\)](#), [Wechsler et al. \(2002\)](#) and [Zhao et al. \(2009\)](#).

More recently, [Ludlow et al. \(2016\)](#); see also [Ludlow et al. 2014](#)) proposed a model in which a halo’s scale radius is determined by the epoch at which a certain fraction of the final halo mass was first assembled into progenitor halos above a certain mass threshold. This approach improves upon those described above by accounting for the effects of the specific merger history of each halo on its concentration, rather than considering just the typical assembly history for halos of a given mass. As such, the approach of [Ludlow et al. \(2016\)](#) is able to capture halo-to-halo variations in concentration at

* Corresponding author: abenson@carnegiescience.edu

fixed halo mass, thereby explaining the origin of scatter in the concentration–mass relation.

Ludlow et al. (2016) demonstrated that this model could accurately predict the concentrations of individual N-body halos given their formation histories (i.e. the set of progenitor halos). This clearly demonstrated that concentration of a given halo is closely connected to the distribution of its progenitor halos.

Benson et al. (2019) applied the Ludlow et al. (2016) model to merger trees constructed using the algorithm proposed by Parkinson et al. (2008), and used this to predict the distribution of concentrations for $z = 0$ halos in different mass intervals. Benson et al. (2019) found that, while the mean of the predicted distribution of concentrations accurately matched that measured from N-body simulations, the scatter in the distribution was significantly smaller than that of the N-body distribution of concentrations, even after introducing some dependence of halo formation histories on large scale environment.

In this work, we hypothesize that at least some of this “missing” scatter in the distribution of concentrations must be due to the fact that the Ludlow et al. (2016) model does not make use of the entirety of the information available in a merger tree, but instead makes use of what is essentially a summary statistic (i.e. the epoch at which a certain mass fraction is assembled into progenitors above a certain mass). Wang et al. (2020) have explored the effects of major and minor mergers on halo concentrations measured from N-body simulations, finding that “merger events induce lasting and substantial changes in halo structures.” Wang et al. (2020) conclude that minor mergers are a source of irreducible scatter in the concentration–mass relation, bolstering our hypothesis.

In this work we therefore develop a model for predicting scale radii which takes into account the entire structure of a merger tree and which we therefore expect to capture more of the scatter in concentration at fixed halo mass.

The inspiration for this model is the work of Vitvitska et al. (2002), who construct a random walk model for the spin parameters (i.e. the dimensionless measure of the internal angular momenta) of halos. Briefly, they assume that whenever two halos merge, the spin angular momentum of the merged system is equal to the sum of the spin angular momenta of the two merging halos, plus the orbital angular momenta of those halos at the point of merging (i.e. when the smaller halo first crosses the virial radius of the larger halo). This assumption is applied at each merging event in a tree to predict the evolution of spin along each branch. Recently, Benson et al. (2020) updated this model and demonstrated that it can provide an excellent match to the distribution of spin parameters measured in N-body simulations, and also gives a reasonable reproduction of the correlation properties of spins across time.

In this work we apply this same approach to predicting halo scale radii and shapes by assuming that energy is similarly (approximately) conserved during halo mergers. This allows us to compute the internal energy of each halo in a merger tree, which we then map into scale radii for each halo. Models of this type take into account the entirety of a halo’s merger history, and incorporate information from mergers across all mass ratios. Importantly, no artificial dis-

inction is drawn between minor and major mergers—the mass ratio of mergers is treated as a continuum.

The remainder of this paper is organized as follows. In §2 we describe our model for halo scale radii, and how we constrain the parameters of this model. In §3 we present results for the distribution of concentrations in different mass intervals compared to measurements from N-body simulations, and explore predictions from our model for the correlation structure of scale radii across time, and correlations between scale radius and halo spin. Finally, in §4 we give our conclusions. We include two appendices. In Appendix A we describe how we model the effects of unresolved accretion, and demonstrate the validity of the approach through a resolution study. In Appendix B we provide the full posterior distribution of our model parameters. The model developed in this work is implemented and available within the open source GALACTICUS toolkit.

2 MODEL FOR SCALE RADII

We begin by constructing merger trees using the algorithm of Parkinson et al. (2008) with parameters given by Benson et al. (2019). As in Benson et al. (2019), we include a modification to the halo branching rates which captures the effects of large scale environment. All trees are rooted in a $z = 0$ halo whose mass, M_0 , is chosen from some distribution (we will describe the distribution of $z = 0$ halo masses in each application of our model below), and are grown backward in time using the Parkinson et al. (2008) algorithm until the halo mass along each branch reaches a pre-defined threshold, which we refer to as the mass resolution, M_{res} . As in Benson et al. (2020) we choose to set $M_{\text{res}} = f_{\text{res}} M_0$, with a fiducial fractional resolution of $f_{\text{res}} = 10^{-3}$. Any progenitor halos with mass less than M_{res} are therefore missing from our merger trees. The effects of these sub-resolution halos are not ignored however, as will be discussed below.

Our model is applicable to any combination of cosmological parameters. In this work we will calibrate our model to the COCO (Hellwing et al. 2016) simulations which assume a cosmology of $(\Omega_m, \Omega_\Lambda, \Omega_b, H_0/\text{km s}^{-1}\text{Mpc}^{-1}, \sigma_8, n_s) = (0.272, 0.728, 0.0446, 70.4, 0.81, 0.967)$. In §3.1.1 we will test our model by comparing to the VSM DPL simulation (Klypin et al. 2016) which assumes a cosmology of $(\Omega_m, \Omega_\Lambda, \Omega_b, H_0/\text{km s}^{-1}\text{Mpc}^{-1}, \sigma_8, n_s) = (0.307, 0.693, 0.0482, 67.77, 0.823, 0.96)$.

For specificity we will assume a Navarro et al. (1997; “NFW”) density profile throughout (although we explore the consequences of instead using an Einasto profile in §3.2, where we show that the our qualitative conclusions are unaffected by the choice of density profile). The NFW profile is given by:

$$\rho(r) = \frac{\rho_s}{(r/r_s)(1+r/r_s)^2} \quad (1)$$

where r_s is the scale radius, and ρ_s is a normalization factor.

Our model relies on determining the internal energy of a halo. We find the energy following the approach of Cole et al. (2000), assuming the halo to be spherical, supported by isotropic velocity dispersion, and in Jeans equilibrium.

The gravitational energy is given by:

$$W = -\frac{G}{2} \left[\int_0^{r_v} \frac{M^2(r)}{r^2} dr + \frac{M^2(r_v)}{r_v} \right], \quad (2)$$

where $M(r)$ is the mass enclosed within a sphere of radius r .

The kinetic energy is given by:

$$T = 2\pi \left[r_v^3 \rho(r_v) \sigma^2(r_v) + \int_0^{r_v} GM(r) \rho(r) r dr \right], \quad (3)$$

where $\sigma(r)$ is the velocity dispersion at radius r is determined from the Jeans equation:

$$\frac{d(\rho\sigma^2)}{dr} = -\rho(r) \frac{GM(r)}{r^2}. \quad (4)$$

Cole et al. (2000) derive the velocity dispersion at r_v by integrating the Jeans equation to $r = \infty$ assuming that the Navarro et al. (1997) profile and Jeans equilibrium apply at all radii.

Importantly, by truncating the halo at r_v in this way the halo is not precisely in virial equilibrium: $2T + W \neq 0$.

The total energy, $E = W + T$, will be a function of the two parameters ρ_s and r_s of the Navarro et al. (1997) profile. Equivalently, we can write $E(M, r_s)$ where $M = M(r_v)$ since the density normalization can be derived from the mass, scale radius, and the choice of density contrast used to define halo mass.

Therefore, the energy of a halo of known mass depends only on r_s —so if we know the energy of the halo the scale radius can be determined. We will next describe how we compute the total energy, E , for each halo in a merger tree.

2.1 Algorithm for scale radii

Beginning with a merger tree we perform a depth-first walk of the tree, visiting each halo in turn. In what follows, we refer to any progenitor halos of the halo currently being visited using subscript “ i ”, with M_i being the virial mass of that progenitor halo, and r_i its virial radius. The total energy of each halo is then computed as follows.

Halos with no resolved progenitors: For these halos we determine a scale radius by assigning a concentration from the mass-concentration-redshift relation¹ proposed by Diemer & Kravtsov (2015). The energy of the halo is then computed using equations (2) and (3).

Halos with one or more progenitors: For halos with one or more resolved progenitor halos, we label progenitors by an index $i = 1$ to N , with $i = 1$ corresponding to the most massive progenitor. We set the energy equal to the sum of the energies of progenitors and the contribution from unresolved accretion:

$$E = \left[\sum_{i=1}^N E_{p,i} (1 + \mu_i)^{-\gamma} + E_u \right] (1 + b), \quad (5)$$

¹ We have checked that our results for scale radii are insensitive to this choice. For example, if we instead assign a fixed concentration of $c = 10$ to halos with no resolved progenitor (such that there is no concentration-mass relation imposed on these halos), our results for $z = 0$ halos are not significantly affected. This implies that, for a sufficiently well-resolved merger history, the final scale radius of a halo is insensitive to the scale radii of its distant progenitors.

where $E_{p,i}$ is the energy of the i^{th} progenitor, $\mu_i = M_i/M_1$, E_u is the energy of unresolved accretion, and b and γ are parameters whose values we will determine by requiring our model to match N-body simulation results.

The parameters b and γ are introduced to account for the approximations made by our model (such as spherical symmetry, Jeans equilibrium, etc.) and to allow it to be calibrated to match results from N-body simulations. We expect each parameter to be of order unity. Specifically, b acts as an overall “boost” factor by which the energy of a halo exceeds that of its progenitors, while γ acts to create an additional dependence of the energy contributed by each progenitor on the mass of that progenitor.

For resolved progenitors we can write $E_{p,i} = E_{p,\text{int},i} + E_{p,\text{orb},i}$, where $E_{p,\text{int},i}$ is the internal energy of the progenitor (which will have already been computed by virtue of the nature of our depth-first tree walk), and $E_{p,\text{orb},i}$ is the orbital energy of the progenitor. To find the orbital energy, for $i > 1$ we select an orbit for each progenitor from the distribution proposed by Jiang et al. (2015) and compute

$$E_{p,\text{orb},i} = \left[-\frac{GM_1 M_i}{r_1} + \frac{1}{2} \frac{M_i v_i^2}{1 + \mu_i} \right], \quad (6)$$

where v_i is the orbital speed of the merging progenitor halo. For the most massive progenitor, $i = 1$, we assume no orbital energy (as this progenitor defines the primary “branch” of the tree into which the other progenitors are merging). Note that, unlike in Benson et al. (2020), where we were concerned about a vector quantity (angular momentum), here we do not need to consider correlations between the orbital angular momenta of infalling satellite halos and that of the primary halo, as this does not affect the energy.

The mass of material accreted in unresolved halos is taken to be $M_u = M_d - \sum_{i=0}^N M_i$, where M_d is the mass of the halo whose energy we are computing. We then set $E_u = \beta M_u (\epsilon_{\text{orbit}} + \epsilon_{\text{internal}})$ where ϵ_{orbit} and $\epsilon_{\text{internal}}$ are given by equations (A4) and (A8) respectively, and β is determined in Appendix A2. Note that β (not to be confused with the parameter b introduced above) is not a free parameter of our model, but is instead fixed by requiring that our algorithm for scale radii be stable with respect to the mass resolution of the merger trees used.

After completing this tree walk, each halo with one or more progenitors in the tree has been assigned a total energy, E , from equation (5). We then step back through the tree and compute the corresponding scale radius such that $E(M, r_s) = E$.

2.2 Calibration

Our model has two free parameters, b and γ . To calibrate these parameters we make use of the distributions of concentration parameter measured from the COCO N-body simulations (Hellwing et al. 2016) by Benson et al. (2019). To do so we generate a sample of merger trees, and compute scale radii for them using the approach described in the previous subsection. When generating these trees we match the cosmological parameters and power spectrum of the COCO simulation, and sample a total of 40,000 $z = 0$ halo masses from the halo mass function between $M_0 = 10^9 M_\odot$ and $10^{13} M_\odot$, growing a tree for each sampled mass.

After building each tree and computing the scale radius of the $z = 0$ halo, we determine the concentration parameter $c_{200c} = r_s/r_{200c}$, where r_{200c} is the radius enclosing a mean density equal to 200 times the critical density, to match the definition used by [Benson et al. \(2019\)](#) when measuring concentrations from the COCO simulations. We then construct distributions of concentrations in seven logarithmically-spaced mass bins spanning the range $9.4 < \log_{10}(M/M_\odot) < 12.4$, matched to the same mass intervals in which distributions of concentrations were measured from the COCO simulations. Within each mass range, we construct a binned histogram of concentrations which is then normalized to provide an estimate of the distribution of concentrations within the mass bin. That is, we compute

$$p_i \equiv \frac{dP_i}{d \log_{10} c_{200c}} = \frac{N_i}{\Delta \log_{10} c_{200c} \sum_j N_j}, \quad (7)$$

where N_i is the number of halos with concentrations falling within the i^{th} bin of concentration, $\Delta \log_{10} c_{200c}$ is the width of each concentration bin, and the sum in the denominator is taken over all concentration bins. As in [Benson et al. \(2019\)](#) we smooth the resulting distributions by a Gaussian with width chosen to match the expected uncertainty in N-body halo concentration estimates ([Benson et al. 2019](#), equation 5). We use the exact same approach to estimate concentration distributions from the COCO simulation (except that there is no need to for the final smoothing step).

Finally, we define the likelihood of our model given the N-body data in each mass interval as:

$$\log \mathcal{L} = -\frac{1}{2} \Delta \mathbf{C}^{-1} \Delta^T, \quad (8)$$

where Δ is a vector of differences between the N-body and model concentration histograms, and \mathbf{C} is a covariance matrix. The covariance matrix is taken to be the sum of that of the N-body halo histogram, and that of the model halo histogram, $\mathbf{C} = \mathbf{C}_{\text{N-body}} + \mathbf{C}_{\text{model}}$. We assume that the uncertainty in the number of halos contributing to each bin is $\sqrt{N_i}$, i.e. we assume Poisson statistics. These uncertainties, for both the N-body and model concentration distributions, are then used to construct the respective covariance matrices, including the off-diagonal terms which arise from the fact that the N_i appear in the denominator of equation (7). Specifically,

$$\mathbf{C} = \mathbf{J} \mathbf{C}' \mathbf{J}^T \quad (9)$$

where \mathbf{J} is the Jacobian matrix:

$$J_{ij} = \frac{dp_i}{dN_j}, \quad (10)$$

and

$$C'_{ij} = \begin{cases} N_i^2 & \text{if } i = j \\ 0 & \text{otherwise.} \end{cases} \quad (11)$$

Additionally, the Gaussian smoothing that was applied to the model histograms is accounted for when computing the covariance matrix for our model.

When constructing the histogram of model halo concentrations we exclude halos which have more than doubled their mass in the last 1.25 crossing times (3.7 Gyr; [Ludlow et al. 2016](#), §2.1.1). This selection criterion was applied to the COCO N-body halos from which concentrations were

measured by [Benson et al. \(2019\)](#) to remove out of equilibrium halos (for which concentration may not be well defined), and so we apply the same selection to halos in our model.

We then run an MCMC simulation to determine the posterior distribution over the parameters b and γ . We follow the same approach in our MCMC methodology as [Benson et al. \(2020\)](#), utilizing 64 parallel chains, and generating proposals using differences between chains. We allow the simulation to progress until all chains are converged. We judge convergence using the Gelman-Rubin statistic, \hat{R} ([Gelman & Rubin 1992](#)), after removing outlier chains (identified using the Grubb's outlier test ([Grubbs 1969](#); [Stefansky 1972](#)) with significance level $\alpha = 0.05$). Convergence is assumed once \hat{R} reaches a value of 1.2 in the parameters of interest, b and γ .

In addition to b and γ , we include several nuisance parameters in our MCMC simulation, which we will marginalize over in the final analysis. All parameters are described below. For b and γ we also detail the priors used, while for nuisance parameters we adopt the same priors as in [Benson et al. \(2020\)](#).

- b : Energies of merging subhalos are multiplied by $1 + b$ (see equation 5). This parameter is therefore expected to be of order unity. We adopt a uniform prior for b between -1 and $+1$.
- γ : This parameter appears as the exponent of the mass-dependent correction to the energy of merging halos (see equations 5 and A1). We adopt a uniform prior between -2 and $+2$.
- (A, a, p) in the [Sheth et al. \(2001\)](#) mass function.
- $(G_0, \gamma_1, \gamma_2)$ in the halo merger rate model of [Parkinson et al. \(2008\)](#).
- (b, γ, σ, μ) in each primary halo mass, and secondary-to-primary mass ratio range in the fitting function for orbital parameters of subhalos of [Jiang et al. \(2015\)](#).

This gives a total of 44 parameters, although as noted, all except b and γ have narrow priors and are included only as nuisance parameters allowing us to marginalize over their uncertainties.

3 RESULTS

Our MCMC simulation reaches convergence after 1,250 steps. We allow it to run for a further 1,116 steps, and find a correlation length in each chain of around 25 steps. Therefore, our post-convergence chains provide approximately 2,800 independent samples from the posterior distribution over our parameters. The full posterior distribution is shown in Fig. B1, and we find $\gamma = 1.518_{-0.036}^{+0.036}$ and $b = (6.730_{-0.247}^{+0.049}) \times 10^{-1}$ when marginalized over all other parameters.

Figure 1 shows the distribution of concentrations in two intervals of $z = 0$ halo mass from our model (yellow points) and from the COCO simulations (blue points), showing an overall very good agreement.

Figure 2 and table 1 show the first four moments of the concentration distribution in each halo mass interval. The mean is reproduced in all mass intervals to better than 0.04 dex. The scatter is systematically underpredicted by

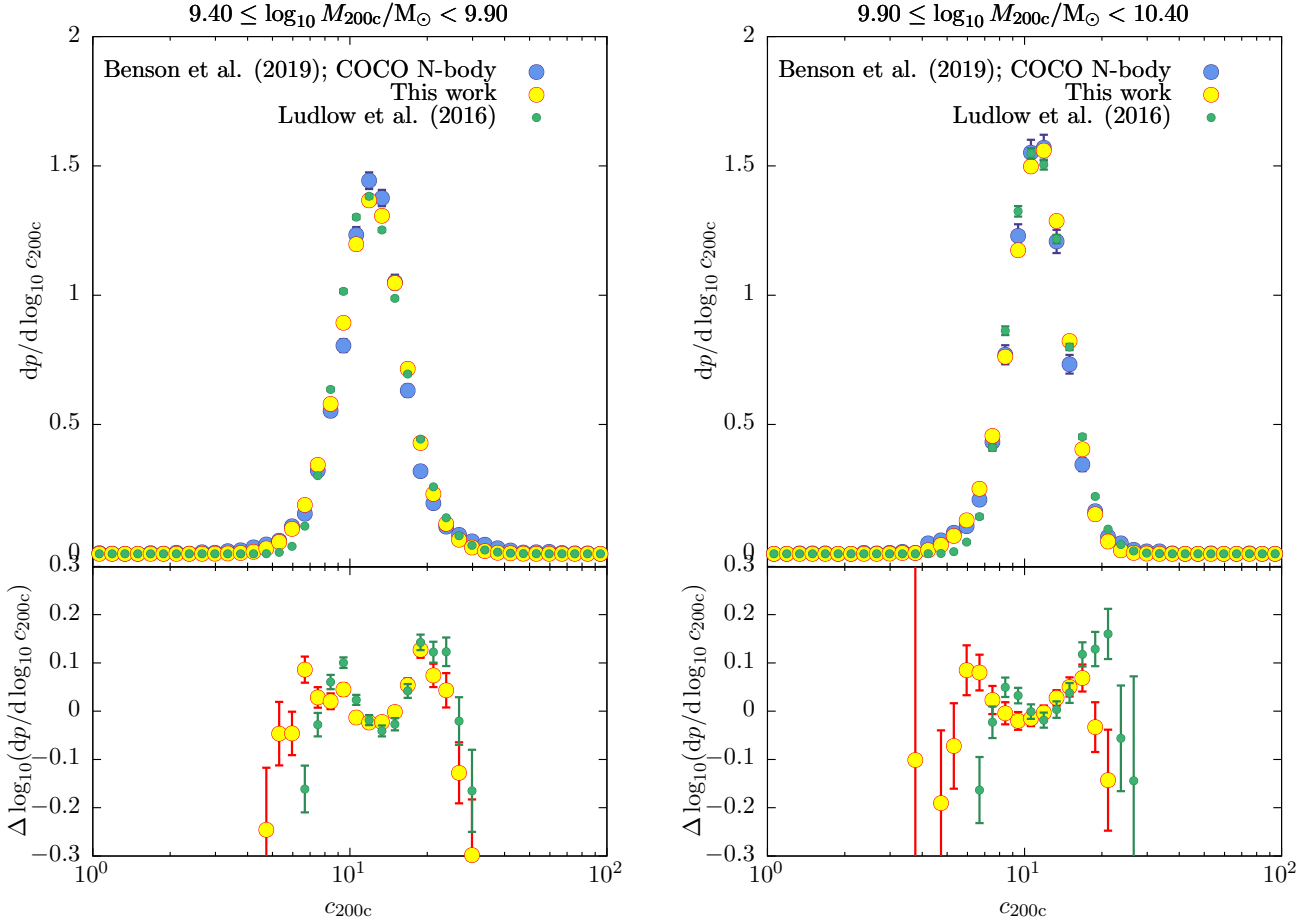


Figure 1. *Upper panels:* Distributions of concentration parameter for $z = 0$ halos in two mass ranges (as indicated above each panel). Blue points show the measured distribution from the COCO N-body simulation from [Benson et al. \(2019\)](#), while yellow points show results from the maximum likelihood model in this work, and smaller green points show results using the model of [Ludlow et al. \(2016\)](#) (using the best-fit parameter values from [Benson et al. 2019](#)). *Lower panels:* The logarithmic residuals between the models of this work and of [Ludlow et al. \(2016\)](#) and the COCO N-body simulation results.

our model, by around 0.02 dex (the underprediction is larger for the higher mass intervals, but for these the uncertainty in the N-body scatter is too large to confirm that these larger discrepancies are real). To examine why, it is informative to look at the next two moments. The N-body distributions have mild negative skewness, which is reasonably well matched by our model. However, the N-body distributions also have significant positive excess kurtosis (i.e. are leptokurtic). While our model also produces leptokurtic concentration distributions they are not leptokurtic enough compared to the N-body distributions. This can be appreciated by a close inspection of Fig. 1 where the N-body results (blue) points can be seen to have excess in the tails of the distribution compared to the results from our model (yellow points). While the measurements of kurtosis for the N-body data have large uncertainties, the discrepancy from our model is significant.

3.0.1 Comparison with Ludlow et al. (2016)

The model of [Ludlow et al. \(2016\)](#) predicts the concentration of a halo utilizing the time at which a given fraction of the halo’s mass was first assembled into progenitors above a given mass threshold. [Benson et al. \(2019\)](#) previously calibrated the parameters of the [Ludlow et al. \(2016\)](#) model using the same merger trees, and the same N-body calibration data set as used in this work.

In the $9.40 \leq \log_{10} M_{200c}/M_{\odot} < 9.90$ mass interval [Benson et al. \(2019\)](#) found a mean of $c_{200c} = 1.077$ and scatter of $\sigma_{\log_{10} c_{200c}} = 0.114$ utilizing the model of [Ludlow et al. \(2016\)](#) together with their model for the dependence of halo merger rates on environment. Our model attains a closer match to both the mean and, significantly, the scatter measured in the N-body simulation than does the [Benson et al. \(2019\)](#) model, although as noted above, our model still does not reproduce the full scatter measured in the N-body halos.

We show the results from the [Ludlow et al. \(2016\)](#) model in Figures 1 and 2 as smaller green points. In Figure 1 it can be seen that the [Ludlow et al. \(2016\)](#) model produces results

Table 1. Moments of the distribution of concentrations, under the assumption of NFW halo profiles. (For an equivalent table under the assumption of Einasto halo profiles, see Table 2.) Each pair of rows shows results for a different $z = 0$ halo mass range, with results from this work shown on a white background and from the COCO N-body measurements from [Benson et al. \(2019\)](#) on a grey background. The first column indicates the halo mass range, while the remaining columns show the mean, scatter (i.e. root-variance), skewness, and (excess) kurtosis. For the N-body results uncertainties arising from the finite number of halos available are found via bootstrapping from the original measurements. Uncertainties due to the finite number of halos used in this work are much smaller and so are not shown. We indicate with “–” cases where the N-body data had too few halos to allow a robust measurement to be made.

Halo mass	Moments of $\log_{10} c_{200c}$			
	Mean	Scatter	Skewness	Kurtosis
$9.40 \leq \log_{10} M_{200c}/M_{\odot} < 9.90$	1.08437	0.13433	−0.03770	0.44587
	1.08366 ± 0.00042	0.15258 ± 0.00600	$−0.07742 \pm 0.09698$	$+3.74604 \pm 0.99892$
$9.90 \leq \log_{10} M_{200c}/M_{\odot} < 10.40$	1.04137	0.11687	−0.38536	0.54178
	1.03958 ± 0.00043	0.13007 ± 0.00768	$−0.41040 \pm 0.06405$	$+3.90800 \pm 2.08336$
$10.40 \leq \log_{10} M_{200c}/M_{\odot} < 10.90$	0.99589	0.10762	−0.43343	0.41786
	1.00375 ± 0.00051	0.12272 ± 0.01842	$−0.43141 \pm 0.11352$	$+5.22451 \pm 4.01680$
$10.90 \leq \log_{10} M_{200c}/M_{\odot} < 11.40$	0.95217	0.10428	−0.54034	0.61359
	0.97634 ± 0.00082	0.12813 ± 0.04245	$−0.09612 \pm 0.22848$	$+5.79007 \pm 5.35354$
$11.40 \leq \log_{10} M_{200c}/M_{\odot} < 11.90$	0.90402	0.10436	−0.60677	0.50302
	0.94719 ± 0.00480	0.16496 ± 0.08039	$−0.09540 \pm 0.47306$	$+3.37100 \pm 3.78467$
$11.90 \leq \log_{10} M_{200c}/M_{\odot} < 12.40$	0.86916	0.10148	−0.37351	−0.13485
	0.90750 ± 0.01905	0.19381 ± 0.13419	$+0.17929 \pm 0.55379$	$+2.62945 \pm 3.91738$
$12.40 \leq \log_{10} M_{200c}/M_{\odot} < 12.90$	0.81733	0.09442	−0.39473	−0.28924
	–	–	–	–

very similar to that of this work—with the notable exception that it significantly underpredicts the tail of N-body halos with low concentrations, while the model described in this work achieves a much better match to this low-concentration tail. This can also be seen in the second panel of Figure 2 which shows the skewness in the concentration distribution as a function of halo mass. The [Ludlow et al. \(2016\)](#) significantly overpredicts skewness at low masses, while the model of this work matches the N-body skewness accurately. At higher masses the uncertainty in the N-body skewness becomes too large to discriminate between the models.

Considering the scatter in concentration, our model produces larger scatter (albeit by a small amount) at all masses except for the highest mass bin, and is therefore closer to the N-body results. The model of [Ludlow et al. \(2016\)](#) performs somewhat better in matching the mean concentration at higher masses. However, this is largely due to the fact that the [Ludlow et al. \(2016\)](#) is positively skewed—the mode of the concentration distribution in the models of [Ludlow et al. \(2016\)](#) and of this work are in close agreement across all halo masses.

The origin of the skewness in the distribution of concentrations at fixed mass is unclear. In the [Ludlow et al. \(2016\)](#) model this must arise from the structure of the merger trees themselves (as this is the only input to the [Ludlow et al. \(2016\)](#) model). The [Ludlow et al. \(2016\)](#) model predicts a significant positive skewness, which, as noted above, is due to a lack of halos in the tail of low concentrations. It is possible that these low-concentration halos arise from merger histories which have significant late-time merging, which would increase their energies, making them less bound (and, therefore, less concentrated). Such late-time merger activity may not be captured by the [Ludlow et al. \(2016\)](#) model, which considers only the time at which a certain fraction of a halo’s final mass was first assembled. In the model presented in this work, such late-time merging *would* affect the halo concentration as we consider the effects of every merging event.

Of the remaining skewness present in our model it is

interesting to ask how much of this arises from the structure of the merger trees, and how much from any skewness in the distribution of merging halo orbital energies. To examine this we ran our model using an artificially modified distribution of merging halo orbital parameters, constructed to have the same mean and variance as the original distribution, but with zero skewness in orbital energy (i.e. we symmetrized the distribution of orbital energies about the mean). We found that this led to only a small increase in skewness, not significantly changing the level of agreement with the N-body data. The skewness in our model must therefore arise from the structure of the merger trees.

Finally, it is interesting to consider the kurtosis predicted by the [Ludlow et al. \(2016\)](#) model. In the top panel of Figure 2 we compare the predicted kurtosis to that measured in N-body simulations. As with the model of this work, [Ludlow et al. \(2016\)](#) predicts a kurtosis much lower than that measured in the N-body simulations, and, in fact, is largely consistent with the kurtosis predicted by the model of this work.

This mismatch in kurtosis could indicate that our model (and that of [Ludlow et al. 2016](#)) are failing to capture some of the extremes of halo formation histories, which might indicate some limitation of either the structure of the merger trees used in this work, or in our model for concentrations. Alternatively, it may be that the kurtosis in the distribution of N-body concentrations may be an artefact of how those concentrations are measured. For example, substantial substructure, or non-sphericity in the N-body halos may bias the measurement of concentrations from them. This is a question which could, and should, be explored, perhaps by an extension of the analysis of [Benson et al. \(2019\)](#) in which realizations of N-body halos with known concentration are generated, and then a fitting procedure is used to recover the concentration, allowing uncertainties inherent in the fitting procedure to be characterized. While [Benson et al. \(2019\)](#) used such an analysis to estimate the contribution of such uncertainties to the scatter in concentration, the same ap-

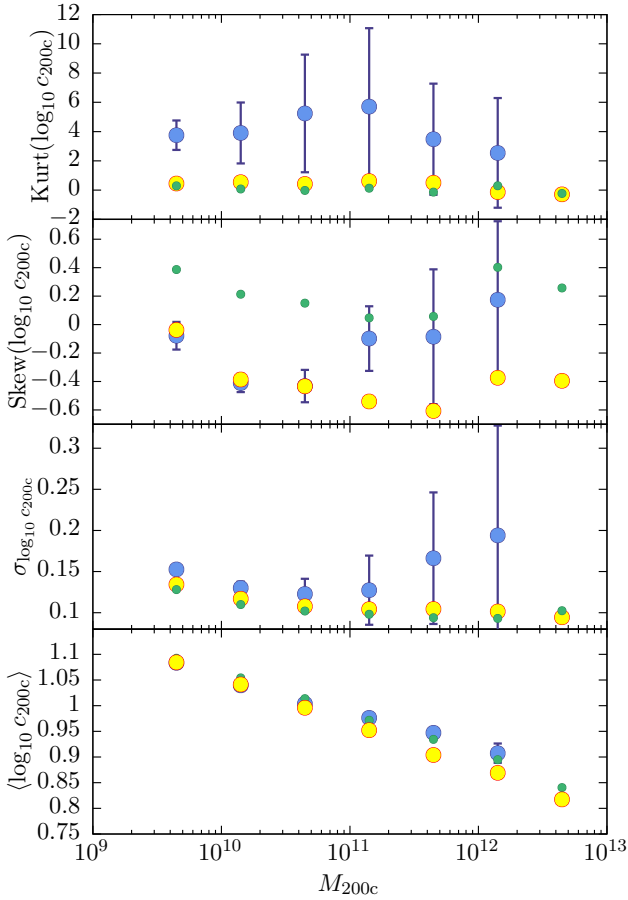


Figure 2. Moments of the distribution of concentrations, under the assumption of NFW halo profiles. Each panel shows a different moment (mean, scatter (i.e. root-variance), skewness, and (excess) kurtosis from bottom to top) as a function of $z = 0$ halo mass, with results from this work shown as yellow points, and from the COCO N-body measurements from [Benson et al. \(2019\)](#) as blue points. Also shown, as smaller green points, are results from the model of [Ludlow et al. \(2016\)](#) (using the best-fit parameter values from [Benson et al. 2019](#)). For the N-body results uncertainties arising from the finite number of halos available are found via bootstrapping from the original measurements. Uncertainties due to the finite number of halos used in this work are much smaller and so are not shown.

proach could be used to explore contributions to kurtosis also, and could incorporate simple models of non-sphericity and substructure also to quantify their contribution to scatter, kurtosis, and other moments of the distribution.

3.1 Tests of the model

Having constrained our model to match the distribution of $z = 0$ halo concentrations as a function of mass, we now explore other statistics predicted by our model and compare them to results from N-body simulations as a way to test the predictive power of our model.

We consider two predictions from our model. In §3.1.1 we examine the autocorrelation function of halo concentra-

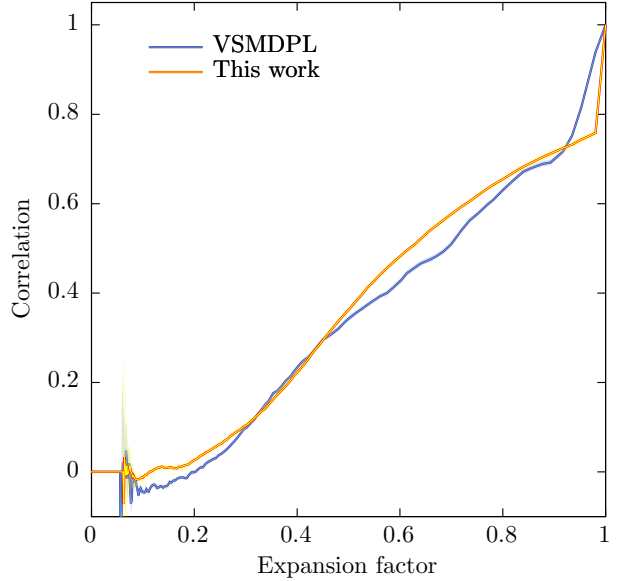


Figure 3. The autocorrelation of halo scale radius as a function of expansion factor for our sample of $z = 0$ halo. The double red line indicates results from the sample of halos extracted from the VSMDPL N-body simulation, with the yellow shaded region indicating bootstrap uncertainties on this quantity.

tions across time, while in §3.1.2 we examine the correlation between halo concentration and halo spin parameter.

For these tests we make use of data from the VSMDPL simulation provided via the [CosmoSim](#) database. From the Rockstar ([Behroozi et al. 2013](#)) halo catalogs derived from the VSMDPL simulation we select $z = 0$ halos with masses greater than $2.74 \times 10^{11} M_{\odot}$, corresponding to 30,000 particles, and their primary progenitors² down to masses of $2.74 \times 10^9 M_{\odot}$, corresponding to 300 particles. This gives a sample of 77,099 halos which are sufficiently well resolved that we can follow their structure back to early times in the simulation.

3.1.1 Auto-correlation function

In Fig. 3 we show the autocorrelation function of normalized halo scale radius (described below) for this sample of N-body halos from the VSMDPL simulation as a function of expansion factor (blue line, with uncertainties determined from bootstrapping indicated by the blue shading).

Since our sample includes halos with a wide range of scale radii, we normalize scale radii to that expected under

² We define “primary progenitor” recursively. Let i label snapshots of the simulation at redshifts z_i such that $z_0 = 0$ and $z_{i+1} > z_i$. The primary progenitor at snapshot i , p_i , is defined as $p_i = \text{mmp}(p_{i-1})$ where $\text{mmp}(p)$ is a function that selects the most massive progenitor of halo p . Note that this means that p_i is not necessarily the most massive halo in a merger tree at snapshot i , but instead corresponds to the halo reached by stepping back through the halo, always moving to the most massive progenitor of the current halo.

the mean concentration-mass relation of [Gao et al. \(2008\)](#), and then compute the autocorrelation function of these normalized scale radii. We follow [Ludlow et al. \(2016; see also Benson et al. 2019\)](#) and exclude halos which have more than doubled their mass in the past 3.7 Gyr in order to exclude systems which may be out of equilibrium.

Measurements of halo concentration (and, therefore, scale radius) from N-body simulations are affected by uncertainties due to the finite number of particles present in the N-body halo, and to the non-smooth, non-spherical nature of cosmological halos. In [Fig. 3](#) the initial rapid drop in the correlation function (from expansion factor $a = 1$ to $a \approx 0.9$) is a consequence of these measurement uncertainties. For $a < 0.9$ the continued decline in the correlation function is driven by real, physical decorrelation of halo scale radii. As can be seen from [Fig. 3](#), the correlation drops to 0.5 at an expansion factor of $a \approx 0.7$, corresponding to a look-back time of $t \approx 4.6$ Gyr. This can be compared to the timescale for linear growth D/\dot{D} (where $D(t)$ is the linear growth factor, and an overdot represents a time derivative) which is the timescale on which we expect cosmological structures to grow, and which is approximately 7 Gyr at $z = 0$. We can conclude that the concentration of a halo changes significantly on a timescale comparable to the timescale of structure growth.

To compute the correlation function using the model from this work we build a set of approximately 36,000 merger trees using parameters sampled from the posterior distribution of our MCMC simulation. We match cosmological and power spectrum parameters to the VSMDPL simulation, and span the same range of masses for $z = 0$ halos as for the VSMDPL simulation. The resolution of each merger trees is set to $M_{\text{res}} = \min(10^{-3}M_0, 2.74 \times 10^9 M_\odot)$ such that all trees resolve progenitors to at least the mass limit for progenitors used in our correlation analysis, and with at least enough resolution to ensure that our concentrations are well-converged. For these trees, we output the primary progenitor at the set of redshifts corresponding to the snapshots available in the VSMDPL simulation.

As our determinations of scale radii for these trees are not affected by the same uncertainties that affect measurements from N-body simulations, we must add noise to our scale radii to mimic this effect in order to permit a fair comparison with the N-body results. [Benson et al. \(2019\)](#) determined the uncertainty for their measurements of concentration from the COCO N-body simulations and provide a fitting function for the uncertainty, as a function of halo particle number and concentration. We adopt this model here, but allow some freedom in the choice of normalization (the lead term in the expression $a(c_{200c})$ in equations 4 & 5 of [Benson et al. 2019](#)) as the details of the way in which scale radii were measured by [Benson et al. \(2019\)](#) and by ROCKSTAR (which was used for VSMDPL) differ. While [Benson et al. \(2019\)](#) found a value of -0.20 for this term for cosmological halos, we find that a value of $+0.20$ is required to match the uncertainties in the VSMDPL ROCKSTAR halo catalogs.

The results are shown in [Fig. 3](#) by the yellow region, which spans the 10th and 90th percentiles of the posterior distribution, with the central line showing the 50th percentile (i.e. median).

The effects of the mimicked N-body uncertainties are

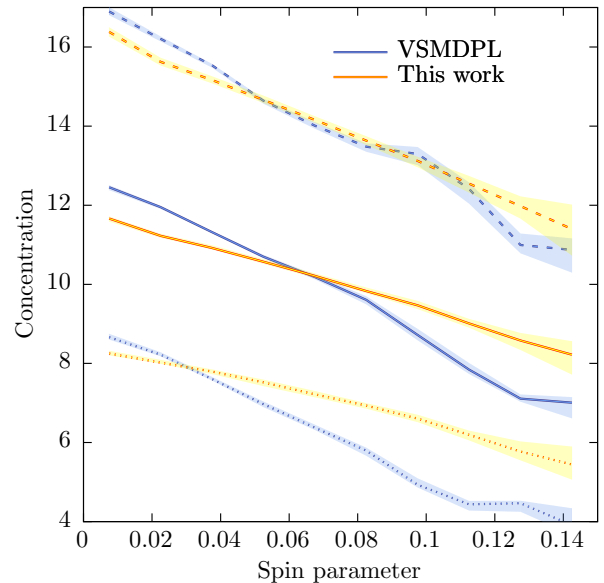


Figure 4. The 10th, 50th, and 90th percentiles (dotted, solid, and dashed lines respectively) of the distribution of concentrations as a function of spin parameter for $z = 0$ halos selected from the VSMDPL N-body simulation (blue lines) and for halos created using the model described in this work, and augmented by the model for halo spin from ([Benson et al. 2020](#); yellow lines). Shaded bands show the uncertainties in these percentiles. In the case of the VSMDPL simulation uncertainties are found by bootstrap resampling of the N-body halos, while in the case of the results from this work the uncertainties are found by marginalizing over the posterior distribution of the model parameters.

clearly seen in the red line, which drops sharply at the first $a < 1$ snapshot. (Note that the VSMDPL line drops over a few snapshots, presumably because some of the noise effects that cause this drop are correlated between snapshots—we do not attempt to model that correlation in our mimicked noise). If this noise is removed from our model scale radii the yellow curve instead declines smoothly.

Once these numerical effects are accounted for, our model closely matches the dependence of the correlation function on expansion factor measured from the VSMDPL simulation, indicating that its predicted evolution of scale radii in time is consistent with N-body results.

3.1.2 Concentration-Spin Correlation

We next examine any possible correlation between halo concentration and spin parameter. [Figure 4](#) shows the 10th, 50th, and 90th percentiles (dotted, solid, and dashed lines respectively) of the distribution of concentrations as a function of spin parameter using the same set of halos from the VSMDPL N-body simulation as used in [§3.1.1](#) (blue lines), as well as from our matched set of merger trees generated using the model developed in this paper (yellow lines), to which we now additionally apply the random-walk model

for halos spins³ developed by [Benson et al. \(2020\)](#), allowing us to simultaneously predict both concentrations and spin parameters. Shaded bands show the uncertainties in these percentiles. In the case of the VSMDPL simulation, uncertainties are found by bootstrap resampling of the N-body halos, while in the case of the results from this work the uncertainties are found by marginalizing over the posterior distribution of the model parameters.

We again mimic the numerical uncertainties in concentrations from the N-body simulation as in §3.1.1, and now also mimic numerical uncertainties in spins using the model of [Benson \(2017\)](#). The [Benson \(2017\)](#) model for spin noise contains two parts: a spin-independent term which describes the random walk in spin as the angular momenta of individual particles are summed, and a spin-dependent term which is driven by the factors of mass, energy, and radius which appear in the definition of spin. Since both this spin-dependent part and the noise in halo concentrations are driven by the same underlying uncertainty in the total number of particles in the halo, we expect them to be correlated. In fact, since the $|E|^{1/2}M^{-5/2}$ term appearing in the definition of halo spin ([Peebles 1969](#)) scales as $M^{-5/3}$, while concentrations scale as $R \propto M^{1/3}$, we expect an upward fluctuation in $M \propto N$ to increase concentration, but decrease spin. We therefore model these error terms as being anti-correlated.

Figure 4 shows a clear correlation between concentration and spin parameter, with higher spin implying lower concentration. This is understandable in the context of our model for halo concentrations coupled with the spin model of [Benson et al. \(2020\)](#). A high spin halo typically results from the merging of a relatively massive halo with large specific angular momentum. Such a halo also has relatively large (i.e. less negative) energy due to the high kinetic energy associated with that large specific angular momentum and high mass—as such it will tend to increase the specific energy of the halo it merges with, thereby lowering its concentration.

Our model predicts a trend of concentration with spin which matches quite closely that measured from the N-body simulation.

3.2 Effects of Choice of Density Profile

Throughout this work we have made use of the NFW ([Navarro et al. 1997](#)) density profile for dark matter halos. More recent works ([Navarro et al. 2004](#); [Gao et al. 2008](#); [Navarro et al. 2010](#)) have suggested that the Einasto (1965) profile is a more accurate description of the density profiles of cosmological cold dark matter halos. While the NFW profile is described by just a single parameter, r_s , (once the total mass and density contrast of the halo are fixed), the Einasto profile requires two parameters, the radius at which the logarithmic slope of the density profile equals -2 , r_{-2} , and a shape parameter, α .

Our model allows us to uniquely determine the density profile of a halo only in the case of a single-parameter family,

such as NFW. Therefore, to explore a two-parameter family such as the Einasto profile we fix the value of the shape parameter α using the fitting function of [Gao et al. \(2008\)](#). We then apply our model to the case of Einasto profiles. We use the most probable *a posteriori* values of the parameters b and γ (and all nuisance parameters) determined from our MCMC simulation. Since that simulation utilized NFW halos we may expect some offset in the results when applied to Einasto profiles.

Fig. 5 shows distributions of concentration parameters for this calculation. There is a small but clear shift to higher concentrations compared to the NFW profile case, while the scatter in concentration is slightly reduced (see Table 2). Our qualitative conclusions are therefore not affected by the choice of density profile. The quantitative agreement with N-body results when using an Einasto profile could be improved by performing a new MCMC simulation to recalibrate b and γ .

4 CONCLUSIONS

We have described a model for predicting the scale radii (or, equivalently, concentrations) of dark matter halos based on their full merging history. The approach is motivated by existing work which demonstrates a clear connection between concentration and halo formation history (e.g. [Ludlow et al. 2016](#)), but utilizes a random walk model in halo energy inspired by similar treatments for halo angular momentum ([Vitvitska et al. 2002](#); [Benson et al. 2020](#)).

When calibrated, this model closely reproduces the mass-dependent distribution of concentrations measured in N-body simulations. By utilizing the entirety of the information available in a halo’s merger tree, our model explains more of the scatter in the concentration-mass relation than previously possible (see, for example, [Benson et al. 2019](#)). Furthermore, we have shown that our model closely matches the auto-correlation function of scale radii across time measured from a high-resolution cosmological N-body simulation, and, when coupled with the random-walk model for halo spins of [Benson et al. \(2020\)](#), also closely matches the correlation between the distribution of concentrations and halo spin parameter measured from that same simulation.

Simulations of non-cold dark matter in which the power spectrum has a cut-off at low masses show a turnover in the concentration-mass relation. As has been shown by [Ludlow et al. \(2016\)](#) such a turnover can be predicted by models which relate the concentration to the assembly history of halos. As such, we expect our model to capture this behavior. We intend to explore such scenarios and confirm this expectation in a future work.

While our model, which is implemented and available within the open source [GALACTICUS](#) toolkit, offers further insight into the physics that determines halo concentrations, it also provides a practical method to assign concentrations to halos with merger histories derived from non-N-body means (e.g. those derived using Press-Schechter-based approaches). Furthermore, since our model is based on a simple physical principle, we expect it to be applicable beyond the cold dark matter scenario to which we have applied it here, in the same way that the [Ludlow et al. \(2016\)](#) model performs well for warm dark matter scenarios also. This will

³ Note that we include the correlations between orbital parameters of merging halos and the spin vector of the halo with which they merge as required by the [Benson et al. \(2020\)](#) model for spins. This has no effect on the concentration model developed in this work.

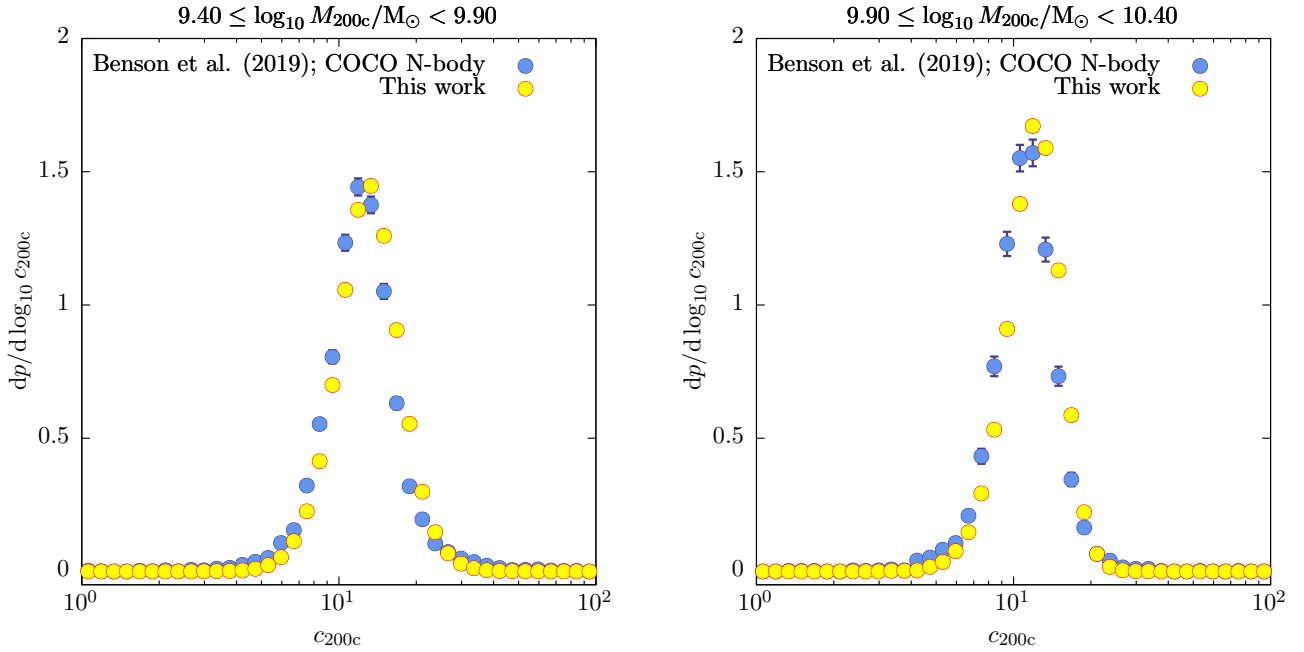


Figure 5. Distributions of concentration parameter for $z = 0$ halos in two mass ranges (as indicated above each panel) using an Einasto density profile in our model. Blue points show the measured distribution from the COCO N-body simulation from [Benson et al. \(2019\)](#), while yellow points show results from the maximum likelihood model in this work.

Table 2. Moments of the distribution of concentrations when dark matter halos are described by the Einasto density profile. Each pair of rows shows results for a different $z = 0$ halo mass range, with results from this work shown on a white background and from the COCO N-body measurements from [Benson et al. \(2019\)](#) on a grey background. The first column indicates the halo mass range, while the remaining columns show the mean, scatter (i.e. root-variance), skewness, and (excess) kurtosis. For the N-body results uncertainties arising from the finite number of halos available are found via bootstrapping from the original measurements. Uncertainties due to the finite number of halos used in this work are much smaller and so are not shown. We indicated with “-” cases where the N-body data had too few halos to allow a robust measurement to be made.

Halo mass	Moments of $\log_{10} c_{200c}$			
	Mean	Scatter	Skewness	Kurtosis
$9.40 \leq \log_{10} M_{200c}/M_{\odot} < 9.90$	1.11174	0.12784	-0.06165	0.49756
	1.08366 ± 0.00041	0.15253 ± 0.00596	-0.07679 ± 0.09654	$+3.73987 \pm 0.99651$
$9.90 \leq \log_{10} M_{200c}/M_{\odot} < 10.40$	1.07119	0.10992	-0.44929	0.68686
	1.03959 ± 0.00043	0.13002 ± 0.00764	-0.41005 ± 0.06403	$+3.89411 \pm 2.07840$
$10.40 \leq \log_{10} M_{200c}/M_{\odot} < 10.90$	1.02692	0.10166	-0.50873	0.53342
	1.00373 ± 0.00051	0.12306 ± 0.01856	-0.43248 ± 0.11532	$+5.29632 \pm 4.00389$
$10.90 \leq \log_{10} M_{200c}/M_{\odot} < 11.40$	0.98158	0.10055	-0.64269	0.84683
	0.97634 ± 0.00082	0.12787 ± 0.04236	-0.09675 ± 0.22818	$+5.74564 \pm 5.36260$
$11.40 \leq \log_{10} M_{200c}/M_{\odot} < 11.90$	0.93336	0.10095	-0.64093	0.41492
	0.94716 ± 0.00482	0.16616 ± 0.08023	-0.08421 ± 0.47342	$+3.50488 \pm 3.84163$
$11.90 \leq \log_{10} M_{200c}/M_{\odot} < 12.40$	0.89613	0.09645	-0.36252	-0.23116
	0.90715 ± 0.01863	0.19223 ± 0.13267	$+0.17263 \pm 0.55505$	$+2.56086 \pm 3.75227$
$12.40 \leq \log_{10} M_{200c}/M_{\odot} < 12.90$	0.83867	0.09151	-0.32343	-0.04665
	-	-	-	-

be invaluable in computing the properties of halos and sub-halos for a wide variety of non-CDM scenarios.

ACKNOWLEDGEMENTS

Work by DG and TJ was supported by the Provost’s Office at Haverford College. TJ thanks the Carnegie Observatories for their support, and Gwen Rudie for organizing the summer intern program, which was funded in part by support from The Rose Hills Foundation and The Ralph M. Parsons

Foundation, within which this work was carried out. AJB and DG thank Marc Kamionkowski for discussions and support during the development of the initial concept for this work, which was carried out with support from the Moore Foundation.

We thank Sownak Bose and Stelios Kazantzidis for valuable discussions. The calculations used in this paper were performed on the *mies* cluster, made available through a generous grant from the Ahmanson Foundation. The MultiDark Database used in this paper and the web application providing online access to it were constructed as part

of the activities of the German Astrophysical Virtual Observatory as result of a collaboration between the Leibniz-Institute for Astrophysics Potsdam (AIP) and the Spanish MultiDark Consolider Project CSD2009-00064. The Bolshoi and MultiDark simulations were run on the NASA's Pleiades supercomputer at the NASA Ames Research Center. The MultiDark-Planck (MDPL) and the BigMD simulation suite have been performed in the Supermuc supercomputer at LRZ using time granted by PRACE.

DATA AVAILABILITY

The data underlying this article are available in Zenodo, at... N-body simulation data from the COCO simulation is publicly available (after registration) at <https://www.cosmosim.org/>. N-body simulation data from the VSM-DPL simulation is publicly available (after registration) at <https://www.cosmosim.org/>.

REFERENCES

- Behroozi P. S., Wechsler R. H., Wu H.-Y., 2013, *ApJ*, 762, 109
- Bellovary J. M., Dalcanton J. J., Babul A., Quinn T. R., Maas R. W., Austin C. G., Williams L. L. R., Barnes E. I., 2008, *ApJ*, 685, 739
- Benson A., Behrens C., Lu Y., 2020, arXiv:2001.09208 [astro-ph], arXiv: 2001.09208
- Benson A. J., 2017, *MNRAS*, 471, 2871
- Benson A. J., Ludlow A., Cole S., 2019, *MNRAS*, 485, 5010
- Bullock J. S., Kolatt T. S., Sigad Y., Somerville R. S., Kravtsov A. V., Klypin A. A., Primack J. R., Dekel A., 2001, *MNRAS*, 321, 559
- Cole S., Lacey C. G., Baugh C. M., Frenk C. S., 2000, *MNRAS*, 319, 168
- Dalal N., Lithwick Y., Kuhlen M., 2010, arXiv e-prints, arXiv:1010.2539
- Diemer B., Kravtsov A. V., 2015, *ApJ*, 799, 108
- Einasto J., 1965, *Trudy Astrofizicheskogo Instituta Alma-Ata*, 5, 87
- Gao L., Navarro J. F., Cole S., Frenk C. S., White S. D. M., Springel V., Jenkins A., Neto A. F., 2008, *MNRAS*, 387, 536
- Gelman A., Rubin D. B., 1992, *Statistical Science*, 7, 457
- Gilman D., Birrer S., Nierenberg A., Treu T., Du X., Benson A., 2019, arXiv e-prints, arXiv:1908.06983
- Gilman D., Du X., Benson A., Birrer S., Nierenberg A., Treu T., 2020, *MNRAS*, 492, L12
- Grubbs F., 1969, *Technometrics*, 11, 1
- Hellwing W. A., Frenk C. S., Cautun M., Bose S., Helly J., Jenkins A., Sawala T., Cytowski M., 2016, *Mon Not R Astron Soc*, 457, 3492
- Jiang F., Dekel A., Freundlich J., van den Bosch F. C., Green S. B., Hopkins P. F., Benson A., Du X., 2020, arXiv e-prints, 2005, arXiv:2005.05974
- Jiang F., Dekel A., Kneller O., Lapiner S., Ceverino D., Primack J. R., Faber S. M., Macciò A. V., et al., 2019, *MNRAS*, 488, 4801
- Jiang L., Cole S., Sawala T., Frenk C. S., 2015, *MNRAS*, 448, 1674
- Klypin A., Yepes G., Gottlöber S., Prada F., Heß S., 2016, *MNRAS*, 457, 4340
- Ludlow A. D., Bose S., Angulo R. E., Wang L., Hellwing W. A., Navarro J. F., Cole S., Frenk C. S., 2016, *MNRAS*, 460, 1214
- Ludlow A. D., Navarro J. F., Angulo R. E., Boylan-Kolchin M.,

- Springel V., Frenk C., White S. D. M., 2014, *MNRAS*, 441, 378
- Navarro J. F., Frenk C. S., White S. D. M., 1996, *ApJ*, 462, 563
- , 1997, *ApJ*, 490, 493
- Navarro J. F., Hayashi E., Power C., Jenkins A. R., Frenk C. S., White S. D. M., Springel V., Stadel J., et al., 2004, *MNRAS*, 349, 1039
- Navarro J. F., Ludlow A., Springel V., Wang J., Vogelsberger M., White S. D. M., Jenkins A., Frenk C. S., et al., 2010, *MNRAS*, 402, 21
- Parkinson H., Cole S., Helly J., 2008, *MNRAS*, 383, 557
- Peebles P. J. E., 1969, *ApJ*, 155, 393
- Sheth R. K., Mo H. J., Tormen G., 2001, *MNRAS*, 323, 1
- Springel V., Wang J., Vogelsberger M., Ludlow A., Jenkins A., Helmi A., Navarro J. F., Frenk C. S., et al., 2008, *MNRAS*, 391, 1685
- Stefansky W., 1972, *Technometrics*, 14, 469
- Vitvitska M., Klypin A. A., Kravtsov A. V., Wechsler R. H., Primack J. R., Bullock J. S., 2002, *ApJ*, 581, 799
- Wang K., Mao Y.-Y., Zentner A. R., Lange J. U., van den Bosch F. C., Wechsler R. H., 2020, arXiv e-prints, 2004, arXiv:2004.13732
- Wechsler R. H., Bullock J. S., Primack J. R., Kravtsov A. V., Dekel A., 2002, *ApJ*, 568, 52
- Zhao D. H., Jing Y. P., Mo H. J., Börner G., 2009, *ApJ*, 707, 354

APPENDIX A: UNRESOLVED ACCRETION

Our merger trees have a finite mass resolution, below which accretion of halos is no longer resolved. Since those unresolved halos would contribute to the energy of the halo with which they merge we must account for their contributions. We first develop an analytic estimate of the energy contributed by unresolved accretion, and then calibrate this model through a resolution study to ensure that our results are independent of merger tree resolution.

A1 Analytic Estimate

We consider the energy provided by halos accreted below the mass resolution of our merger trees. On average such halos will have an orbital energy per unit mass of (see equation 6)

$$\epsilon_{\text{orbit}} = \left[-\frac{GM_1}{R_1} + \frac{1}{2} \frac{\langle v^2 \rangle}{1 + \mu} \right] (1 + \mu)^{-\gamma}, \quad (\text{A1})$$

where $\langle v^2 \rangle$ is the mean squared velocity of virial crossing orbits, and $\mu = M/M_1$ with M being the mass of the unresolved halo, and M_1 is the mass of the most massive progenitor.

In general we expect $\mu \ll 1$, but we can nevertheless account for this dependence. Assuming a power-law halo mass function for the unresolved halos, $dN/dM \propto M^{-a}$ with $a \approx 1.9$ (e.g. Springel et al. 2008), we can write:

$$\epsilon_{\text{orbit}} = -C_\phi \frac{GM_1}{R_1} + C_K \frac{1}{2} \frac{\langle v^2 \rangle}{1 + \mu_{\text{res}}}, \quad (\text{A2})$$

where $\mu_{\text{res}} = M_{\text{res}}/M_0$,

$$C_\phi = (2 - a) \mu_{\text{res}}^{-2+a} B \left(\frac{\mu_{\text{res}}}{1 + \mu_{\text{res}}}; 2 - a, -2 + a + \gamma \right), \quad (\text{A3})$$

and

$$C_K = (2 - a) \mu_{\text{res}}^{-2+a} B \left(\frac{\mu_{\text{res}}}{1 + \mu_{\text{res}}}; 2 - a, -1 + a + \gamma \right), \quad (\text{A4})$$

where $B()$ is the beta-function.

For the internal energy of each unresolved halo we can write:

$$E_{\text{int}}(M) = -s(M) \frac{GM^2}{R} (1 + \mu)^{-\gamma} \quad (\text{A5})$$

where $s(M)$ depends weakly on mass via the mass dependence of the density profile. If we assume that all accreted halos have the same virial density, then $R = (3M/4\pi\bar{\rho})^{1/3}$, so that

$$E_{\text{int}}(M) = -s(M)G \left(\frac{4\pi\bar{\rho}}{3} \right)^{1/3} M^{5/3} (1 + \mu)^{-\gamma}, \quad (\text{A6})$$

then the mean internal energy per unit mass of accreted subresolution halos is then

$$\epsilon_{\text{int}} = \int_0^{M_{\text{res}}} E_{\text{int}}(M) M^{-a} dM \bigg/ \int_0^{M_{\text{res}}} M M^{-a} dM. \quad (\text{A7})$$

From an analysis of halos generated in higher resolution merger trees we find that $s(M) \propto M^{-c}$ with $c \approx 0.03$. The internal energy per unit mass of accreted subresolution halo is then

$$\begin{aligned} \epsilon_{\text{int}} &= (2 - a - c)/(8/3 - a - c) \\ &\quad \times {}_2F_1[(\gamma, 8/3 - a - c), (11/3 - a - c), -\mu_{\text{res}}^{-1}] \\ &\quad \times E_{\text{int}}(M_{\text{res}})/M_{\text{res}}, \end{aligned} \quad (\text{A8})$$

where ${}_2F_1()$ is a hypergeometric function.

The total energy contributed by unresolved accretion is then taken to be

$$E_{\text{unres}} = \beta [\epsilon_{\text{int}} + \epsilon_{\text{orb}}] (1 + b) M_{\text{unres}}, \quad (\text{A9})$$

where M_{unres} is the increase in mass of a halo which is *not* accounted for by resolved progenitor halos, b is a parameter of our model (introduced in §2) which represents an overall boost in the energy of a halo relative to its progenitors, and $\beta \sim 1$ is a parameter which we introduce to allow us to calibrate this analytic estimate of the energy of unresolved halos.

The parameter β introduced above should be chosen such that the energies (and, therefore, concentrations) of halos are insensitive to changes in the resolution of the merger tree used to characterize the halo's assembly. In the next subsection we will determine an appropriate value for β through a resolution study.

A2 Resolution Study

In the above we introduced a parameter, β , which multiplies our analytic estimate of the energy contributed by unresolved halos. The value of β should be of order unity, and should be chosen such that the mean concentration (at a given halo mass) predicted by our model is independent of the chosen merger tree mass resolution. By exploring different values of β and applying our model to merger trees constructed with different mass resolutions we find that a value of 0.55 gives stable results, as shown in Fig. A1.

The yellow line in Fig. A1 shows the mean concentration predicted (for halos in the mass range indicated above each panel) as a function of the mass resolution parameter, $f_{\text{resolution}}$. The results are essentially independent of resolution, indicating that our model for unresolved accretion works.

It should be noted that the analytic estimate of the energy contributed by unresolved accretion in §A1 estimates only the mean of this contribution—we do not attempt to estimate the scatter in this quantity. However, the blue lines in Fig. A1 show that the scatter in concentration is also independent of merger tree mass resolution, even though we neglect the scatter contributed by unresolved accretion. Since the mass function of accreted halos rises steeply with decreasing halo mass, the law of large numbers implies that the actual energy contributed by unresolved accretion onto a halo will be close to the mean expectation.

APPENDIX B: POSTERIOR DISTRIBUTION

Figure B1 shows the posterior distribution over the model parameters determined from our MCMC simulation described in §2, with nuisance parameters not shown. Both parameters are well-constrained by the N-body data. It is also apparent that their values are strongly correlated in the posterior distribution.

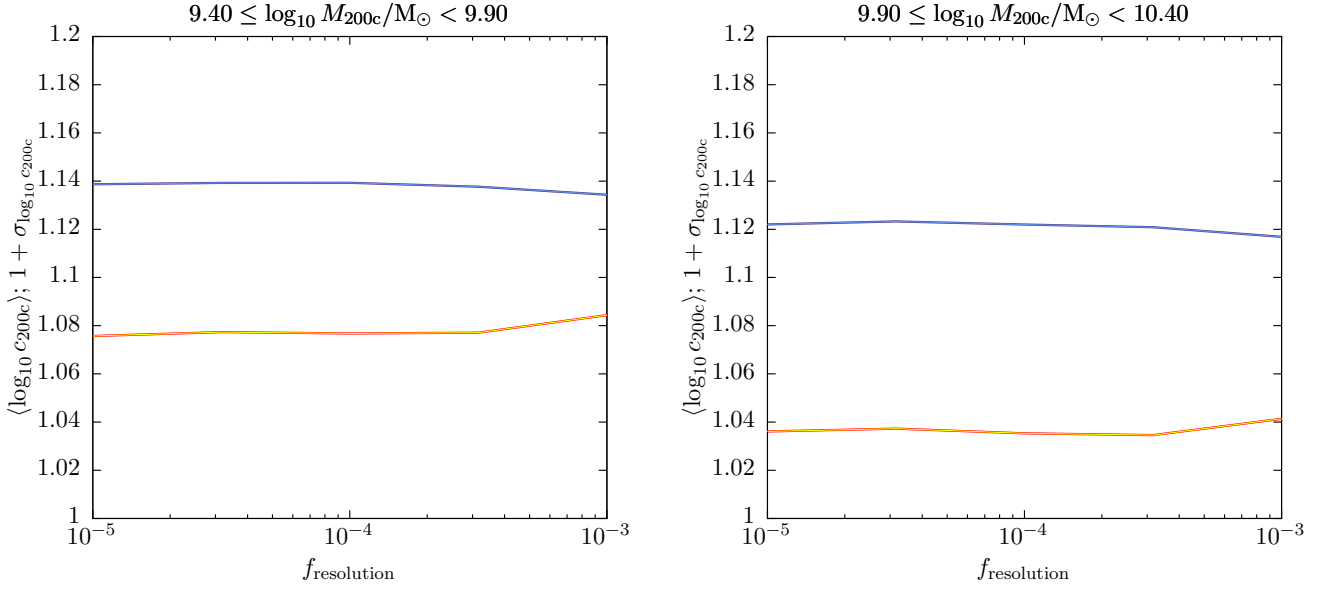


Figure A1. The mean (yellow line) and root-variance (blue line) of the distribution of concentrations for $z = 0$ halos in two mass ranges (as indicated above each panel) as a function of the merger tree resolution.

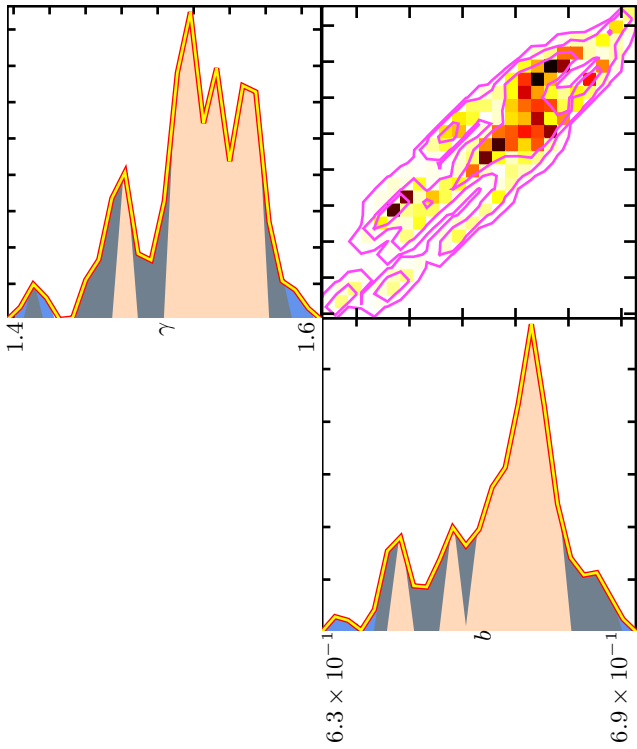


Figure B1. The posterior distribution over the model parameters b and γ . (Nuisance parameters are not shown.) The off-diagonal panel shows the posterior distribution over both model parameters, while on-diagonal panels show the posterior distribution over individual model parameters. In the off-diagonal panel, colours show the probability density running from white (low probability density) to dark red (high probability density). Contours are drawn to enclose 99.7%, 95.4%, and 68.3% of the posterior probability when ranked by probability density (i.e. the highest posterior density intervals). In on-diagonal panels the curve indicates the probability density. Shaded regions indicate the 68.3%, 95.4%, and 99.7% highest posterior density intervals.